

# Concurrent multiscale computational modeling for dense dry granular materials interfacing deformable solid bodies

Richard A. Regueiro and Beichuan Yan

**Abstract** A method for concurrent multiscale computational modeling of interfacial mechanics between granular materials and deformable solid bodies is presented. It involves two main features: (1) coupling discrete element and higher order continuum finite element regions via an overlapping region; and (2) implementation of a finite strain micromorphic pressure sensitive plasticity model as the higher order continuum model in the overlap region. The third main feature, adaptivity, is not currently addressed, but is considered for future work. Single phase (solid grains) and dense conditions are limitations of the current modeling. Extensions to multiple phases (solid grains, pore liquid and gas) are part of future work. Applications include fundamental grain-scale modeling of interfacial mechanics between granular soil and tire, tool, or penetrometer, while properly representing far field boundary conditions for quasi-static and dynamic simulation.

## 1 Introduction

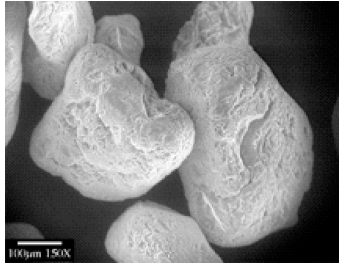
Granular materials are commonly found in nature and industrial processes, and are composites of three phases: solids, liquids, and gases. We limit the modeling currently to single phase (solid grains) and dense materials (average coordination number  $\approx 5$ ). Examples include metallic powders (for powder metallurgy), pharmaceutical pills, agricultural grains (in silo flows), dry soils (sand, silt, gravel), and lunar and martian regolith (soil found on the surface of the Moon and Mars), for instance. We are interested primarily in modeling the grain to macro-continuum scale response in the large shear deformation interface region between a granular material and deformable solid body. Such interface can be between a granular soil (e.g.,

---

Richard A. Regueiro  
University of Colorado at Boulder, Boulder, CO, USA, e-mail: regueiro@colorado.edu

Beichuan Yan  
University of Colorado at Boulder, Boulder, CO, USA e-mail: beichuan.yan@colorado.edu

sand, Fig.1(a)) and a tire(Fig.2(a)), tool (e.g., bucket, Fig.2(b)), or cone penetrometer (Fig.1(b)).



(a) image courtesy of Khalid Alshibli,  
Louisiana State University



(b) [1]

**Fig. 1** (a) Sand grains at 150 $\times$ . (b) Cone penetrometers.

Granular materials remain an unmastered class of materials with regard to modeling their spectrum of mechanical behavior in a physically-based manner across several orders of magnitude in length-scale. They may transition in an instant from deforming like a solid to flowing like a fluid or gas and vice versa. Examples of such physical transition are the flow of quartz grains around and at the tip of a driven cone penetrometer penetrating sand, the shoveling of sand or gravel by a tractor bucket, and the flow of agricultural grains from the bulk top region through the bottom chute in a silo, for instance. These examples each involve material regions where relative neighbor particle motion is ‘large’ (flowing like a fluid or gas) and regions where relative neighbor particle motion is ‘small’ (deforming like a solid).

It is too computationally intensive to account for the grain-scale properties and intergranular constitutive behavior within a physics-based simulation (e.g., discrete element (DE) model) to understand fundamentally the mechanics in a large shear deformation interface region between deformable solid bodies and granular materials. Grain-scale properties include grain size, shape, sphericity, morphology, stiffness, strength, and surface friction, while intergranular constitutive behavior accounts for contact behavior and grain fracture/crushing, for instance. High fidelity particle DE computations that account for these features are expensive, requiring their application be restricted to regions of large shearing at the interface between granular media and a solid body. Boundary effects on the outer simulation boundaries of an assembly of particles interacting with the solid body will render the computational results questionable, because fictitious forces and wave reflections will occur at these outer boundaries of the box of particles, thus influencing in a numerically-artificial manner the actual interface-region mechanics (see section 1.1). To resolve the issue properly, it is necessary to introduce multiscale methods that correctly combine (1) efficient finite element (FE) and/or meshfree based continuum methods used in regions where phenomenological constitutive relationships are accurate, with (2) DE



(a) Mars exploration rover: tire interaction with Martian soil (photo source NASA)



(b) loader bucket scooping gravel (www.dymaxinc.com)

**Fig. 2** (a) Soil-tire, and (b) soil-tool interface problems.

models used in regions where granular physics must be represented accurately (e.g., in the granular soil-tool, soil-tire, or soil-track interface region). The use of multiscale methods offers immediate payoff because the fewer discrete particles needed to simulate the interaction, the faster physics-based simulations can be conducted. As a result, more “what-if” scenarios can be simulated and more uncertainties in grain-scale material parameters can be investigated by simulation, providing “error bars” on the physics-based simulation results. To make the multiscale approach feasible for granular media, an open research question must be addressed: how to maintain a fundamental granular physics representation in the large shear deformation interface region as the solid body shears through the granular material. At the heart of the question is how to achieve adaptability and coupling of the computational scheme to convert from continuum to particle representation around the solid body, as it shears through the granular material, and perform particle to continuum conversion in spatial regions where particles are less sheared or have stopped flowing, and thus a continuum representation is appropriate.

Therefore, the focus of the current research is to bridge grain-scale properties and mechanics to the macro-scale continuum behavior in a large shear deformation interface region between a deformable solid body (e.g., metal scoop, rubber tire, or metal track) and a dense cohesionless granular material (e.g., dry sand or gravel). A multiscale approach is presented to provide fundamental physics-based simulation consisting of (i) FE or rigid body mechanics for the solid body (scoop/tire/track) and DE for the granular material in the large shear deformation interface region (cf. Fig.3), and (ii) FE-DE for the representation of the granular material in the transition/coupling region. The transition (overlap region in the Fig.3) provides proper boundary conditions (BCs) on the physics-based computational discretization (i.e., proper BCs on the DE simulation region).

Ultimately, a fundamental understanding of granular physics interacting with a solid body can lead to improved design of devices for granular soil-machine tool

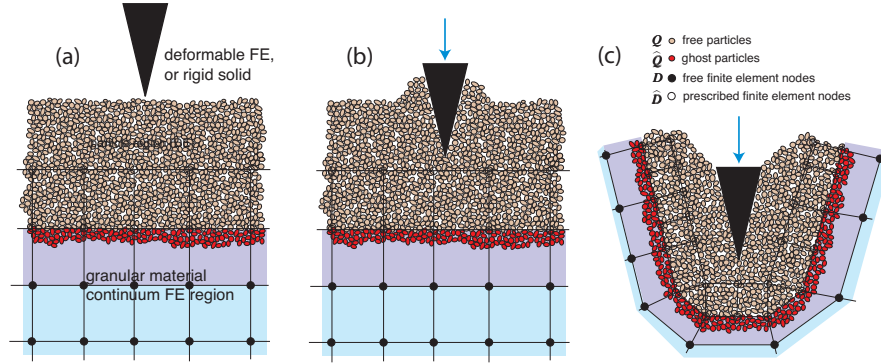


**Fig. 3** Illustration of adaptivity and coupling. In (a), a deformable or rigid solid body approaches the granular material, and in (b) it begins to shear/penetrate the granular material in the DE particle region. In (c), the solid body has sheared the particle region enough that the FE mesh is re-meshed adaptively and the particle region is extended. Adaptivity is addressed in future work.

and soil-tire interaction, and the interpretation of granular soil-penetrometer shear resistance interaction.

### 1.1 Motivation: artificial boundary effects

A penetration test is simulated quasi-statically to demonstrate artificial boundary effects on a DE simulation. The penetrator is modeled using a larger ellipsoidal particle, and the boundaries are composed of fixed spherical particles, shown in Fig.4. Three different-sized containers are used, number of equal-sized particles being 2760, 4260 and 6088, respectively, with ellipsoidal particle radii  $2.5 \times 2.0 \times 1.5$ mm. Parameters for the DE simulation are shown in Table 1.

**Table 1** Parameters of particles and numerical computation.

Young's modulus $E$ (Pa)	$2.9 \times 10^{10}$
Poisson's ratio $\nu$	0.25
specific gravity $G_s$	2.65
interparticle coef. of friction $\mu$	0.5
interparticle contact damping ratio $\xi$	5%
particle radii (m)	0.0015 ~ 0.0025
background damping ratio	dynamic relaxation
time step $\Delta t$ (sec)	$5.0 \times 10^{-6}$

The vertical force-displacement curves are plotted in Fig.4(c) for the penetrator particle. It can be found that the penetrator force increases as penetration increases. For a smaller container, the force has a larger value because of the boundary effect, as

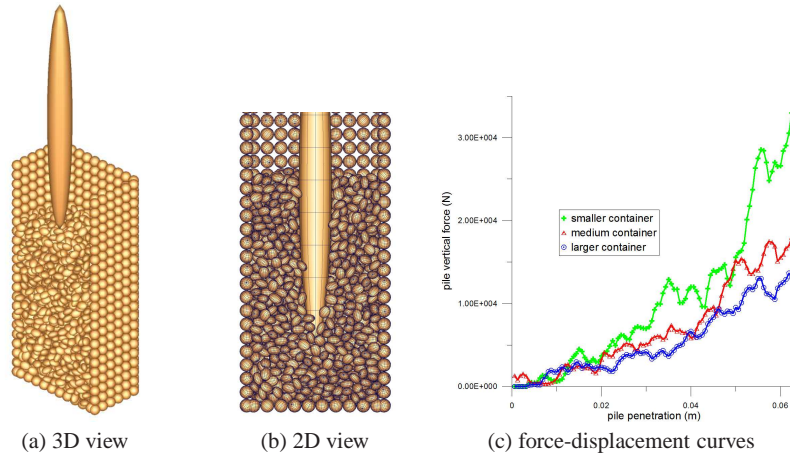


**Fig. 4** Cross-sectional view of penetration, and force-displacement curves.

expected. The question then becomes how to make the shearing DE domain around a deformable solid body as small as possible without introducing artificial boundary effects. This is the overall goal of the research.

An outline of the remainder of the chapter is as follows: section 2 provides a literature review; 3 a summary of balance equations for a particle and micropolar continuum representation of a granular material and their coupling [2]; 4 a method for coupling DE to FE facets [3] and numerical example; 5 a summary; and 6 mention of ongoing and future work.

## 2 Literature Review

The literature review briefly covers work done on micromechanical modeling for granular materials, and computational methods for coupling particle and continuum representations of granular materials.

### 2.1 *Micromechanical continuum models for dense dry granular materials*

Apparently Reynolds [4] was the first to study granular materials at the grain scale, and coined the term “dilatancy” in the process. Others followed [5, 6] with attempts to relate continuum concepts like stress and strain to grain-scale behavior. Conferences were held to focus on micromechanical modeling of granu-

lar materials (this is not a complete list) [7, 8, 9, 10, 11]. The development of continuum relations like stress-strain equations based on micromechanical models of granular materials has spanned nearly five decades and continues today [12, 13, 14, 15, 16, 17, 18, 19, 20]. These micromechanically-based models attempt to bridge the grain to continuum scale mechanics of granular materials within the framework of continuum mechanics and constitutive theory. Furthermore, it has been proposed for granular materials composed of cohesionless, stiff particles (like spherical glass beads) to enhance the continuum to account for particles displacements and rotations (and couple stresses), in essence developing gradient and micropolar continuum models of granular material based on grain-scale mechanics [21, 22, 23, 24, 25, 26, 27, 28, 29, 30, 31]. Many of these approaches consider only elastic deformation of particle assemblies (no breaking of existing particle contacts and slippage at contacts), small strain kinematics, spherical particles, and rotational degrees of freedom (i.e., micropolar; except [24, 26, 28] who included higher-gradient terms).

The micropolar theories applied to stiff, cohesionless particulate materials have gained popularity based on the microstructural observation that in addition to particle translation and sliding, the particles may rotate and roll. It is not sufficient to limit the kinematics of the ‘microstructural view’ (representative volume) of a single particle or cluster of particles to rigid rotation. A representative microscopic volume of granular material—whether the particles are nearly rigid or deformable—will exhibit not only micro-rotation but also micro-shear and micro-stretch (micro-dilatation and micro-compaction). Such additional degrees of freedom within the mathematical framework for micromorphic continuum theories [32] give more realistic bridging kinematics between deformable and rigid particle mechanics and its continuum representation than a micropolar theory would provide.

## ***2.2 Computational particle/continuum coupling***

As continuum micromechanical models were being developed, many recognized the role computers could play in simulating the discrete grain-scale response of granular materials. Such an approach has been called a Distinct Element Method or Discrete Element Method (DEM) [33, 34, 35, 36, 37, 38, 39, 40] (not a complete list). Certain DEM approaches model directly the physical grain size of the material, while others approximate the continuum as an assembly of particles approximating the continuum response discretely, wherein the particles have arbitrary size and thus provide an arbitrary internal length scale. Few approaches have coupled DEM and FEM for modeling deformation and flow of dense dry granular materials accounting for the physical particle size, i.e. truly micromechanically coupled models [41, 42, 43, 44]. These methods approach the coupling issue, however, as a contact/interface problem between discrete particles and finite element facets and not as overlapping regions of the same material, which an approach coupling particle and continuum representations of the same material should do. Examples of such approaches have

been demonstrated for coupled atomistic-continuum regions [45, 46, 47]. Section 3.3 shows the extension of the approach by Klein and Zimmerman [47] to coupled overlapping particle and continuum regions, wherein significant differences have mainly to do with the DE representation of particles (with rotation and frictional sliding, as opposed to molecular dynamics for atoms) and inelastic micromorphic constitutive model for the continuum (and its associated FE implementation). The approach by Xiao and Belytschko [46] is also being considered, which could be somewhat simpler to implement.

Unit cell methods like that by Feyel and Chaboche [48] provide a method to up-scale underlying micromechanical simulations (such as DE) to a macro-scale simulation (such as FE). Belytschko et al. [49] extended the method to modeling fracture. They recognized the complexities and limitations of unit cell methods as they are currently formulated, implemented, and applied. Feyel [50] stated that, in addition to the periodicity assumption for the micro-structure (impossible to model localized deformation), the mechanical response near boundaries was not modeled properly. As a result, these methods are not well suited for modeling the interfacial mechanics of soil-tire, tool, or penetrometer interface conditions. The overlaying FE mesh would quickly become too distorted and require continuous remeshing, aside from the fact that the grain-scale DE mechanics would be influenced by the overlaying continuum mechanical response (through their coupling). The methods are useful, however, in up-scaling fracture or shear banding in a material, but not for interfacial mechanics, as far as we can tell.

### **3 Particle and continuum representations and their coupling**

The balance of linear and angular momentum equations are presented for particle and continuum representations of a dense dry granular material. A strategy for coupling these equations within an overlap region (Fig.6) is summarized in section 3.3.

#### ***3.1 Particle mechanics and Discrete Element Method***

The balance of linear and angular momentum for a system of stiff elastic particles in contact may be written as [33]

$$\begin{aligned}
\mathbf{M}^Q \ddot{\mathbf{Q}} + \mathbf{C}^Q \dot{\mathbf{Q}} + \mathbf{F}^{INT,Q}(\mathbf{Q}) &= \mathbf{F}^{EXT,Q} \quad (1) \\
\mathbf{M}^Q &= \mathbf{A}_{\delta=1}^N \mathbf{m}_\delta^Q; \quad \mathbf{m}_\delta^Q = \begin{bmatrix} \mathbf{m}_\delta & \mathbf{0} \\ \mathbf{0} & \mathbf{I}_\delta \end{bmatrix} \\
\mathbf{F}^{INT,Q} &= \mathbf{A}_{\delta=1}^N \mathbf{f}_\delta^{INT,Q}; \quad \mathbf{f}_\delta^{INT,Q} = \sum_{\varepsilon=1}^{n_c} \begin{bmatrix} \mathbf{f}^{\varepsilon,\delta} \\ \mathbf{r}^{\varepsilon,\delta} \times \mathbf{f}^{\varepsilon,\delta} \end{bmatrix} \\
\mathbf{F}^{EXT,Q} &= \mathbf{A}_{\delta=1}^N \mathbf{f}_\delta^{EXT,Q}; \quad \mathbf{f}_\delta^{EXT,Q} = \begin{bmatrix} \mathbf{f}^{EXT,\delta} \\ \boldsymbol{\ell}^{EXT,\delta} \end{bmatrix}
\end{aligned}$$

where  $\mathbf{M}^Q$  is the mass and rotary inertia matrix for a system of  $N$  particles,  $\mathbf{m}_\delta^Q$  is the mass and rotary inertia matrix for particle  $\delta$ ,  $\mathbf{m}_\delta$  is the mass matrix for particle  $\delta$ ,  $\mathbf{I}_\delta$  is the rotary inertia matrix for particle  $\delta$ ,  $\mathbf{A}_{\delta=1}^N$  is an assembly operator to obtain the system matrices from the individual particle matrices and contact vectors,  $\mathbf{C}^Q = a\mathbf{M}^Q$  the mass and rotary inertia proportional damping matrix with proportionality constant  $a$  (used in a dynamic relaxation solution method for quasi-static problems, but otherwise set to zero),  $\mathbf{F}^{INT,Q}$  the internal force and moment vector associated with  $n_c$  particle contacts which is a nonlinear function of particle displacements and rotations when particles slide with friction,  $\mathbf{f}_\delta^{INT,Q}$  the resultant internal force and moment vector for particle  $\delta$ ,  $\mathbf{f}^{\varepsilon,\delta}$  the internal force vector for particle  $\delta$  at contact  $\varepsilon$ ,  $\mathbf{r}^{\varepsilon,\delta} \times \mathbf{f}^{\varepsilon,\delta}$  the internal moment vector at the centroid of particle  $\delta$  due to force at contact  $\varepsilon$  with moment arm  $\mathbf{r}^{\varepsilon,\delta}$ ,  $\mathbf{F}^{EXT,Q}$  the assembled external force and moment vector,  $\mathbf{f}_\delta^{EXT,Q}$  the external body force and moment vector for particle  $\delta$ ,  $\mathbf{f}^{EXT,\delta}$  the external body force vector at the centroid of particle  $\delta$ , and  $\boldsymbol{\ell}^{EXT,\delta}$  the external body moment vector at the centroid of particle  $\delta$ .  $\mathbf{Q}$  is the generalized degree of freedom (dof) vector for particle displacements and rotations

$$\mathbf{Q} = [\mathbf{q}_\delta, \mathbf{q}_\varepsilon, \dots, \mathbf{q}_\eta, \boldsymbol{\theta}_\delta, \boldsymbol{\theta}_\varepsilon, \dots, \boldsymbol{\theta}_\eta]^T, \quad \delta, \varepsilon, \dots, \eta \in \mathcal{A} \quad (2)$$

where  $\mathbf{q}_\delta$  is the displacement vector of particle  $\delta$ ,  $\boldsymbol{\theta}_\delta$  its rotation vector, and  $\mathcal{A}$  is the set of free particles. In general, a superscript  $Q$  denotes a variable associated with particle motion, whereas a superscript  $D$  will denote a variable associated with continuum deformation. Further details of assembling the matrices and vectors in (1) from the individual particle and particle contact contributions are not given here, as they are well established in the literature.

With regard to putting the particle mechanics and DE implementation into a form amenable to energy partitioning in the coupled particle-continuum overlap region, we consider an energy formulation of the balance equations using Lagrange's equation of motion. It may be stated as

$$\frac{d}{dt} \left( \frac{\partial T^Q}{\partial \dot{\mathbf{Q}}} \right) - \frac{\partial T^Q}{\partial \mathbf{Q}} + \frac{\partial F^Q}{\partial \mathbf{Q}} + \frac{\partial U^Q}{\partial \mathbf{Q}} = \mathbf{F}^{EXT,Q} \quad (3)$$

where  $T^Q$  is the kinetic energy,  $F^Q$  the dissipation function, and  $U^Q$  the potential energy, such that

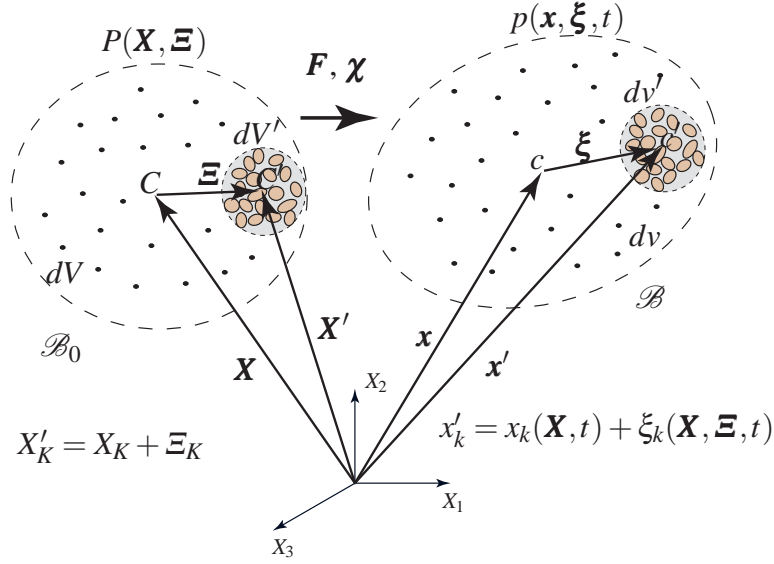


**Fig. 5** Material points  $P(\mathbf{X}, \Xi)$  and  $p(\mathbf{x}, \xi, t)$  in reference and current configurations  $\mathcal{B}_0$  and  $\mathcal{B}$ , respectively, centroids of macro-element  $C$  and  $c$  and micro-element  $C'$  and  $c'$ , relative micro-element position vectors  $\Xi$  and  $\xi$ , differential macro-element volumes  $dV$  and  $dv$  and micro-element volumes  $dV'$  and  $dv'$ . Because of linear kinematics assumption,  $\mathcal{B}_0 \approx \mathcal{B}$ , etc.

$$T^Q = \frac{1}{2} \dot{\mathbf{Q}} \mathbf{M}^Q \dot{\mathbf{Q}}, \quad F^Q = aT^Q, \quad U^Q(\mathbf{Q}) = \int_0^Q \mathbf{F}^{INT, Q}(\mathbf{S}) d\mathbf{S} \quad (4)$$

The dissipation function  $F^Q$  is written as a linear function of the kinetic energy  $T^Q$ , which falls within the class of damping called Rayleigh damping (pg. 130 [51]). Carrying out the derivation in (3), and using the Second Fundamental Theorem of Calculus for  $\partial U^Q / \partial \mathbf{Q}$ , leads to (1).

### 3.2 Micropolar continuum and Finite Element Method

Following the formulation of Eringen [52], we present the balance of linear and angular momentum equations and finite element formulation for a small strain micropolar continuum (i.e., stiff particles with small frictional sliding in overlap region). For clarity of presentation, index tensor notation is used, and Cartesian coordinates are assumed.

The kinematics are reviewed in Fig.5. A micro-element differential volume  $dV'$  (and  $dV'$  in reference configuration<sup>1</sup>) is located by a relative position vector  $\xi_k$  from the centroid  $c$  of the macro-element material point with position  $x_k$  in the current configuration (and relative position vector  $\Xi_K$  from the centroid  $C$  of the macro-element material point with position  $X_K$  in the reference configuration). A micro-deformation tensor  $\chi_{kK}$  relates the reference to current relative position vectors as  $\xi_k = \chi_{kK}(\mathbf{X}, t)\Xi_K$  (summation of repeated indices implied). For small strain micropolar kinematics, the micro-deformation tensor takes the form

$$\chi_{kK} = \delta_{kK} + \varepsilon_{kMK}\Phi_M \quad (5)$$

where  $\delta_{kK}$  is the Kronecker delta,  $\varepsilon_{kMK}$  is the permutation tensor, and  $\Phi_M$  is the micro-rotation vector in the reference configuration. Then the micro-element relative position vector becomes

$$\xi_k = \delta_{kK}\Xi_K + \varepsilon_{kMK}\Phi_M\Xi_K \quad (6)$$

Because of linear kinematics, the reference and current configuration micro-rotation vectors are approximately equal  $\boldsymbol{\varphi} \approx \boldsymbol{\Phi}$ , where  $\varphi_k$  is the micro-rotation vector in the current configuration. Equation (6) states that a micro-element relative position vector  $\boldsymbol{\xi}$  at the deformed macro-element centroid denoted by  $\mathbf{x}$  (cf. Fig.5), involves a parallel translation of  $\boldsymbol{\Xi}$  and rotation through  $\boldsymbol{\Phi} \times \boldsymbol{\Xi}$  (where  $\times$  is the vector cross product). Refer to Eringen [52] for more details.

The balance equations for linear and angular momentum may be written as

$$\sigma_{Ik,l} + \rho b_k - \rho \dot{v}_k = 0 \quad (7)$$

$$m_{Ik,l} + \varepsilon_{kmn}\sigma_{mn} + \rho \ell_k - \rho \dot{\beta}_k = 0 \quad (8)$$

where  $\sigma_{Ik}$  is the unsymmetric Cauchy stress tensor over body  $\mathcal{B}$ ,  $\rho$  is the mass density,  $b_k$  is a body force per unit mass,  $v_k$  is the spatial velocity vector,  $m_{Ik}$  is the unsymmetric couple stress,  $\varepsilon_{kmn}$  is the permutation operator,  $\ell_k$  is the body couple per unit mass,  $\beta_k$  is the intrinsic spin per unit mass, indices  $k, l, \dots = 1, 2, 3$ , and  $(\bullet)_{,l} = \partial(\bullet)/\partial x_l$  denotes partial differentiation with respect to the spatial coordinate  $x_l$ . The micro-gyration vector  $v_l$  for linear kinematics is written as

$$v_l = \dot{\varphi}_l, \quad \dot{v}_l = \dot{\dot{\varphi}}_l \quad (9)$$

Introducing  $w_k$  and  $\eta_k$  as weighting functions for the macro-displacement vector  $u_k$  and micro-rotation vector  $\varphi_k$ , respectively, we apply the Method of Weighted Residuals to formulate the partial differential equations in (7) and (8) into weak form [53]. The weak, or variational, equations then result as

---

<sup>1</sup> Because of the assumption of linear kinematics, small rotations and strains, the reference and current configurations are nearly the same.

$$\int_{\mathcal{B}} \rho w_k \dot{v}_k dv + \int_{\mathcal{B}} w_{k,l} \sigma_{lk} dv = \int_{\mathcal{B}} \rho w_k b_k dv + \int_{\Gamma_t} w_k t_k da \quad (10)$$

$$\int_{\mathcal{B}} \rho \eta_k \dot{\beta}_k dv + \int_{\mathcal{B}} \eta_{k,l} m_{lk} dv - \int_{\mathcal{B}} \eta_k \varepsilon_{kmn} \sigma_{mn} dv = \int_{\mathcal{B}} \rho \eta_k \ell_k dv + \int_{\Gamma_r} \eta_k r_k da \quad (11)$$

where  $\mathcal{B}$  is the volume of the continuum body,  $t_k = \sigma_{lk} n_l$  is the applied traction on the portion of the boundary  $\Gamma_t$  with outward normal vector  $n_l$ , and  $r_k = m_{lk} n_l$  is the applied surface couple on the portion of the boundary  $\Gamma_r$ .

The weak equations (10) and (11) may be approximated in Galerkin form [53], whereby the discretization parameter  $h$  implies a discrete approximation, in this case finite element discretization. Introducing shape functions  $N_a^u$  and  $N_b^\phi$  for the macro-displacement  $u_k^h$  and micro-rotation  $\phi_l^h$  vectors, respectively, and assuming the micro-inertia is approximately constant for small strains and rotations (micro-inertia  $j_{lk}$  is nearly constant, and  $\beta_k^h \approx j_{lk} \phi_l^h$ ), we may write the interpolations and derivatives as

$$u_k^h = \sum_{a=1}^{n_{en}^u} N_a^u d_{k(a)}, \quad \dot{v}_k^h = \sum_{a=1}^{n_{en}^u} N_a^u \dot{d}_{k(a)} \quad (12)$$

$$w_k^h = \sum_{a=1}^{n_{en}^u} N_a^u c_{k(a)}, \quad w_{k,l}^h = \sum_{a=1}^{n_{en}^u} (N_a^u)_{,l} c_{k(a)} \quad (13)$$

$$\phi_l^h = \sum_{b=1}^{n_{en}^\phi} N_b^\phi \phi_{l(b)}, \quad \dot{\phi}_l^h = \sum_{b=1}^{n_{en}^\phi} N_b^\phi \dot{\phi}_{l(b)} \quad (14)$$

$$\eta_k^h = \sum_{b=1}^{n_{en}^\phi} N_b^\phi e_{k(b)}, \quad \eta_{k,l}^h = \sum_{b=1}^{n_{en}^\phi} (N_b^\phi)_{,l} e_{k(b)} \quad (15)$$

where  $d_{k(a)}$  is the displacement vector at node  $a$ ,  $\phi_{l(b)}$  is the rotation vector at node  $b$ ,  $c_{k(a)}$  is the displacement weighting function vector at node  $a$ ,  $e_{k(b)}$  is the rotation weighting function vector at node  $b$ ,  $n_{en}^u$  is the number of element nodes associated with interpolating the continuum macro-displacement vector, and  $n_{en}^\phi$  is the number of element nodes associated with interpolating the continuum micro-rotation vector. It is assumed that the shape functions and integrals are expressed in natural coordinates for an isoparametric formulation, but such details are omitted and can be found in the textbook by Hughes [53]. Substituting these approximations into the Galerkin form, accounting for essential boundary conditions, and recognizing that the nodal weighting function values are arbitrary (except where essential boundary conditions are applied, and nodal weighting function values are zero), we arrive at a coupled matrix form of the linear and angular momentum balance equations as

$$\mathbf{M}^u \ddot{\mathbf{d}} + \mathbf{F}^{INT,u}(\mathbf{d}, \boldsymbol{\phi}) = \mathbf{F}_b + \mathbf{F}_t \quad (16)$$

$$\mathbf{M}^\phi \ddot{\boldsymbol{\phi}} + \mathbf{F}^{INT,\phi}(\mathbf{d}, \boldsymbol{\phi}) = \mathbf{F}_\ell + \mathbf{F}_r \quad (17)$$

where matrices and vectors are assembled from their element contributions using a finite element assembly operator [53] as

$$\mathbf{M}^u = \mathbf{A}_{e=1}^{n_{el}} \mathbf{m}^{e,u}, \quad \mathbf{m}^{e,u} = \int_{\mathcal{B}^e} \rho (\mathbf{N}^{e,u})^T \mathbf{N}^{e,u} dv \quad (18)$$

$$\mathbf{M}^\phi = \mathbf{A}_{e=1}^{n_{el}} \mathbf{m}^{e,\phi}, \quad \mathbf{m}^{e,\phi} = \int_{\mathcal{B}^e} \rho (\mathbf{N}^{e,\phi})^T \mathbf{j} \mathbf{N}^{e,\phi} dv \quad (19)$$

$$\mathbf{F}^{INT,u}(\mathbf{d}, \boldsymbol{\phi}) = \mathbf{A}_{e=1}^{n_{el}} \mathbf{f}^{e,INT,u}, \quad \mathbf{f}^{e,INT,u} = \int_{\mathcal{B}^e} (\mathbf{B}^{e,u})^T \boldsymbol{\sigma}(\mathbf{d}^e, \boldsymbol{\phi}^e) dv \quad (20)$$

$$\mathbf{F}^{INT,\phi}(\mathbf{d}, \boldsymbol{\phi}) = \mathbf{A}_{e=1}^{n_{el}} \mathbf{f}^{e,INT,\phi} \quad (21)$$

$$\mathbf{f}^{e,INT,\phi} = \int_{\mathcal{B}^e} (\mathbf{B}^{e,\phi})^T \mathbf{m}(\mathbf{d}^e, \boldsymbol{\phi}^e) dv - \int_{\mathcal{B}^e} (\mathbf{N}^{e,\phi})^T \boldsymbol{\sigma}^\varepsilon(\mathbf{d}^e, \boldsymbol{\phi}^e) dv$$

$$\mathbf{F}_b = \mathbf{A}_{e=1}^{n_{el}} \mathbf{f}_b^{e,EXT,u}, \quad \mathbf{f}_b^{e,EXT,u} = \int_{\mathcal{B}^e} \rho (\mathbf{N}^{e,u})^T \mathbf{b} dv \quad (22)$$

$$\mathbf{F}_\ell = \mathbf{A}_{e=1}^{n_{el}} \mathbf{f}_\ell^{e,EXT,\phi}, \quad \mathbf{f}_\ell^{e,EXT,\phi} = \int_{\mathcal{B}^e} \rho (\mathbf{N}^{e,\phi})^T \boldsymbol{\ell} dv \quad (23)$$

$$\mathbf{F}_t = \mathbf{A}_{e=1}^{n_{el}} \int_{\Gamma_t^e} (\mathbf{N}^{e,u})^T \mathbf{t} da, \quad \mathbf{F}_r = \mathbf{A}_{e=1}^{n_{el}} \int_{\Gamma_r^e} (\mathbf{N}^{e,\phi})^T \mathbf{r} da \quad (24)$$

where  $\mathbf{A}_{e=1}^{n_{el}}$  is the element assembly operator,  $n_{el}$  is the number of elements,  $\mathbf{N}_e^u$ ,  $\mathbf{N}_e^\phi$ ,  $\mathbf{j}$ ,  $\mathbf{B}_e^u$ ,  $\boldsymbol{\sigma}$ ,  $\mathbf{d}^e$ ,  $\boldsymbol{\phi}^e$ ,  $\mathbf{B}_e^\phi$ ,  $\mathbf{m}$ ,  $\boldsymbol{\sigma}^\varepsilon$ ,  $\mathbf{b}$ ,  $\boldsymbol{\ell}$ ,  $\mathbf{t}$ , and  $\mathbf{r}$  are the element matrix and vector forms of  $N_a^u$ ,  $N_b^\phi$ ,  $j_{lk}$ ,  $(N_a^u)_{,l}$ ,  $\sigma_{lk}$ ,  $d_{k(a)}$ ,  $\phi_{l(b)}$ ,  $(N_b^\phi)_{,l}$ ,  $m_{lk}$ ,  $\varepsilon_{kmn} \sigma_{mn}$ ,  $b_k$ ,  $\ell_k$ ,  $t_k$ , and  $r_k$ , respectively.

Introducing a generalized nodal degree of freedom vector  $\mathbf{D}$ , the coupled micropolar linear and angular momentum balance equations are written as

$$\mathbf{M}^D \ddot{\mathbf{D}} + \mathbf{F}^{INT,D}(\mathbf{D}) = \mathbf{F}^{EXT,D} \quad (25)$$

$$\mathbf{M}^D = \begin{bmatrix} \mathbf{M}^u & \mathbf{0} \\ \mathbf{0} & \mathbf{M}^\phi \end{bmatrix}, \quad \mathbf{D} = \begin{bmatrix} \mathbf{d} \\ \boldsymbol{\phi} \end{bmatrix}$$

$$\mathbf{F}^{INT,D} = \begin{bmatrix} \mathbf{F}^{INT,u} \\ \mathbf{F}^{INT,\phi} \end{bmatrix}, \quad \mathbf{F}^{EXT,D} = \begin{bmatrix} \mathbf{F}_b + \mathbf{F}_t + \mathbf{F}_g^u \\ \mathbf{F}_\ell + \mathbf{F}_r + \mathbf{F}_g^\phi \end{bmatrix} \quad (26)$$

With regard to putting the continuum micropolar mechanics and finite element implementation into a form amenable to energy partitioning in the coupled particle-continuum overlap region, we consider an energy formulation of the balance equations using Lagrange's equation of motion. It may be stated as

$$\frac{d}{dt} \left( \frac{\partial T^D}{\partial \dot{\mathbf{D}}} \right) - \frac{\partial T^D}{\partial \mathbf{D}} + \frac{\partial F^D}{\partial \dot{\mathbf{D}}} + \frac{\partial U^D}{\partial \mathbf{D}} = \mathbf{F}^{EXT,D} \quad (27)$$

where  $T^D$  is the kinetic energy,  $F^D$  the dissipation function, and  $U^D$  the potential energy, such that

$$T^D = \frac{1}{2} \dot{\mathbf{D}} \mathbf{M}^D \dot{\mathbf{D}}, \quad F^D = 0, \quad U^D(\mathbf{D}) = \int_{\mathbf{0}}^{\mathbf{D}} \mathbf{F}^{INT,D}(\mathbf{S}) d\mathbf{S} \quad (28)$$

Carrying out the derivation in (27) leads to (25), assuming constant inertia  $\mathbf{M}^D$ .

### 3.3 Coupling method

An aspect of the computational concurrent multiscale modeling approach is to couple regions of material represented by particle DE to regions of material represented by continuum FE. Another aspect is to bridge the particle mechanics to a continuum representation using finite strain micromorphic plasticity (see [54, 55]), whereas the small strain micropolar continuum is a simple approximation of stiff particles with small frictional sliding in the overlap region. The coupling implementation will allow arbitrarily overlapping particle and continuum regions in a single “hand-shaking” or overlap region such that fictitious forces and wave reflections are minimized in the overlap region. In theory, for nearly homogeneous deformation, if the particle and continuum regions share the same region (i.e., are completely overlapped), the results should be the same as if the overlap region is a subset of the overall problem domain (cf. Fig.6). This will serve as a future benchmark problem for the numerical implementation. The coupling implementation extends to particle mechanics and micropolar continuum the “bridging scale decomposition” proposed by Wagner and Liu [45] and modifications thereof by Klein and Zimmerman [47] (see references therein for further background on these atomistic continuum methods).

#### 3.3.1 Kinematics

Here, a summary of the kinematics of the coupled regions is given, following the illustration shown in Fig.6. It is assumed that the finite element mesh covers the domain of the problem in which the material is behaving more solid-like, whereas in regions of large relative particle motion (fluid-like), a particle mechanics representation is used (DE). In Fig.6, discrete domains are defined, such as the pure particle domain (no overlapping FE mesh) as  $\mathcal{B}^{DE}$ , the FE domain  $\mathcal{B}^h = \hat{\mathcal{B}}^h \cup \tilde{\mathcal{B}}^h \cup \bar{\mathcal{B}}^h$ , where  $\hat{\mathcal{B}}^h$  is the overlapping FE domain where nodal dofs are completely prescribed by the underlying particle DE,  $\tilde{\mathcal{B}}^h$  the overlapping FE domain where particle DE motions and nodal dofs are prescribed and free nodal dofs exist, and  $\bar{\mathcal{B}}^h$  the pure continuum FE domain with no underlying particles. The goal is to have the overlap region  $\hat{\mathcal{B}}^h \cup \tilde{\mathcal{B}}^h$  as close to the region of interest (e.g., penetrometer skin, bucket,

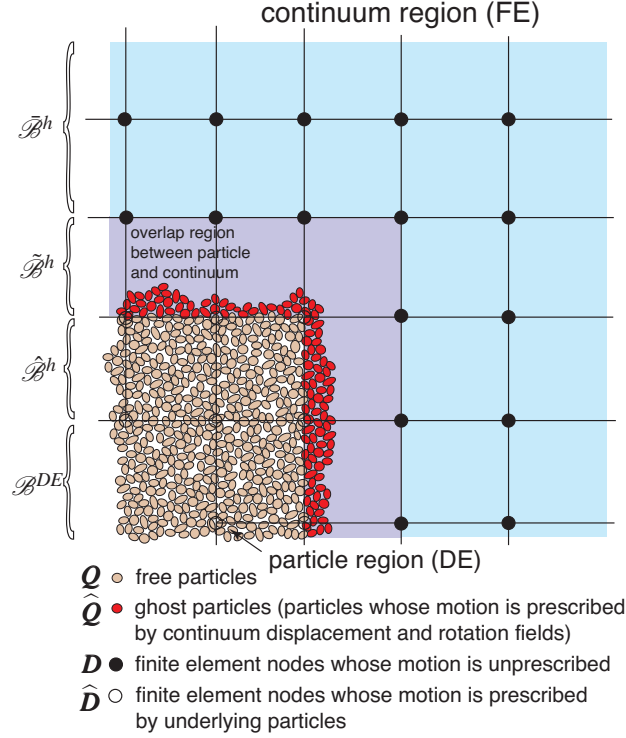


**Fig. 6** Two-dimensional illustration of the coupling between particle and continuum regions. The purple background denotes the FE overlap region  $\tilde{\mathcal{B}}^h$  with underlying ghost particles, aqua blue the FE continuum region  $\hat{\mathcal{B}}^h$  with no underlying particles, and white background (with brown particles) the free particle region  $\hat{\mathcal{B}}^h \cup \mathcal{B}^{DE}$ . In summary, the finite element domain  $\mathcal{B}^h$  is the union of pure continuum FE domain  $\hat{\mathcal{B}}^h$ , overlapping FE domain with underlying ghost particles  $\tilde{\mathcal{B}}^h$ , and overlapping FE domain with underlying free particles  $\hat{\mathcal{B}}^h$ , such that  $\mathcal{B}^h = \hat{\mathcal{B}}^h \cup \tilde{\mathcal{B}}^h \cup \hat{\mathcal{B}}^h$ . The pure particle domain with no overlapping FE domain is indicated by  $\mathcal{B}^{DE}$ .

or tire tread) as to minimize the number of particles, and thus computational effort. Following some of the same notation presented in [47], we define a generalized dof vector  $\check{Q}$  for particle displacements and rotations in the system as

$$\check{Q} = [q_\alpha, q_\beta, \dots, q_\gamma, \theta_\alpha, \theta_\beta, \dots, \theta_\gamma]^T, \quad \alpha, \beta, \dots, \gamma \in \mathcal{A} \quad (29)$$

where  $q_\alpha$  is the displacement vector of particle  $\alpha$ ,  $\theta_\alpha$  its rotation vector, and  $\mathcal{A}$  is the set of all particles. Likewise, the finite element nodal displacements and rotations are written as

$$\check{D} = [d_a, d_b, \dots, d_c, \phi_d, \phi_e, \dots, \phi_f]^T \quad (30)$$

where  $a, b, \dots, c \in \mathcal{N}$ ,  $d, e, \dots, f \in \mathcal{M}$ ,  $d_a$  is the displacement vector of node  $a$ ,  $\phi_d$  is the rotation vector of node  $d$ ,  $\mathcal{N}$  is the set of all nodes, and  $\mathcal{M}$  is the set of

finite element nodes with rotational degrees of freedom, where  $\check{\mathcal{M}} \subset \check{\mathcal{N}}$ . In order to satisfy the boundary conditions for both regions, the motion of the particles in the overlap region (referred to as “ghost particles,” cf. Fig.6) is prescribed by the continuum displacement and rotation fields, and written as

$$\widehat{\mathbf{Q}} = [\mathbf{q}_\alpha, \mathbf{q}_\beta, \dots, \mathbf{q}_\gamma, \boldsymbol{\theta}_\alpha, \boldsymbol{\theta}_\beta, \dots, \boldsymbol{\theta}_\gamma]^T, \quad \alpha, \beta, \dots, \gamma \in \widehat{\mathcal{A}}, \quad \widehat{\mathcal{A}} \in \widehat{\mathcal{B}}^h \quad (31)$$

while the unprescribed (or free) particle displacements and rotations are

$$\mathbf{Q} = [\mathbf{q}_\delta, \mathbf{q}_\varepsilon, \dots, \mathbf{q}_\eta, \boldsymbol{\theta}_\delta, \boldsymbol{\theta}_\varepsilon, \dots, \boldsymbol{\theta}_\eta]^T, \quad \delta, \varepsilon, \dots, \eta \in \mathcal{A}, \quad \mathcal{A} \in \widehat{\mathcal{B}}^h \cup \mathcal{B}^{DE} \quad (32)$$

where  $\widehat{\mathcal{A}} \cup \mathcal{A} = \check{\mathcal{A}}$  and  $\widehat{\mathcal{A}} \cap \mathcal{A} = \emptyset$ . Likewise, the displacements and rotations of nodes overlaying the particle region are prescribed by the particle motion and written as

$$\widehat{\mathbf{D}} = [\mathbf{d}_a, \mathbf{d}_b, \dots, \mathbf{d}_c, \boldsymbol{\phi}_d, \boldsymbol{\phi}_e, \dots, \boldsymbol{\phi}_f]^T \quad (33)$$

where  $a, b, \dots, c \in \widehat{\mathcal{N}}, d, e, \dots, f \in \widehat{\mathcal{M}}, \widehat{\mathcal{N}}, \widehat{\mathcal{M}} \in \widehat{\mathcal{B}}^h \cup \widehat{\mathcal{B}}^h$ , while the unprescribed (or free) nodal displacements and rotations are

$$\mathbf{D} = [\mathbf{d}_m, \mathbf{d}_n, \dots, \mathbf{d}_s, \boldsymbol{\phi}_t, \boldsymbol{\phi}_u, \dots, \boldsymbol{\phi}_v]^T \quad (34)$$

where  $m, n, \dots, s \in \mathcal{N}, t, u, \dots, v \in \mathcal{M}, \mathcal{N}, \mathcal{M} \in \widehat{\mathcal{B}}^h \cup \widehat{\mathcal{B}}^h$ ,  $\widehat{\mathcal{N}} \cup \mathcal{N} = \check{\mathcal{N}}, \widehat{\mathcal{N}} \cap \mathcal{N} = \emptyset, \widehat{\mathcal{M}} \cup \mathcal{M} = \check{\mathcal{M}}$ , and  $\widehat{\mathcal{M}} \cap \mathcal{M} = \emptyset$ . Referring to Fig.6, the prescribed particle motions  $\widehat{\mathbf{Q}}$  can be viewed as constrained boundary particles on the free particle region, and likewise the prescribed finite element nodal displacements and rotations  $\widehat{\mathbf{D}}$  can be viewed as constrained boundary nodes on the finite element mesh in the overlap region.

In general, the displacement vector of a particle  $\alpha$  can be represented by the finite element interpolation of the continuum macro-displacement field  $\mathbf{u}^h$  evaluated at the particle centroid  $\mathbf{x}_\alpha$ , such that

$$\mathbf{u}^h(\mathbf{x}_\alpha, t) = \sum_{a \in \check{\mathcal{N}}} N_a^u(\mathbf{x}_\alpha) \mathbf{d}_a(t) \quad \alpha \in \check{\mathcal{A}} \quad (35)$$

where  $N_a^u$  are the shape functions associated with the continuum displacement field  $\mathbf{u}^h$ . Recall that  $N_a^u$  have compact support and thus are only evaluated for particles with centroids that lie within an element containing node  $a$  in its domain. In DE, particle dofs (translations and rotations) are tracked at the particle centroids, as are resultant forces and moments (from forces acting at contacts). For example, we can write the prescribed displacement of ghost particle  $\alpha$  as

$$\mathbf{q}_\alpha(t) = \mathbf{u}^h(\mathbf{x}_\alpha, t) = \sum_{a \in \check{\mathcal{N}}} N_a^u(\mathbf{x}_\alpha) \mathbf{d}_a(t) \quad \alpha \in \widehat{\mathcal{A}} \quad (36)$$

Likewise, particle rotation vectors can be represented by the finite element interpolation of the continuum micro-rotation field  $\boldsymbol{\phi}^h$  evaluated at the particle centroid  $\mathbf{x}_\alpha$ , such that

$$\boldsymbol{\phi}^h(\mathbf{x}_\alpha, t) = \sum_{b \in \check{\mathcal{M}}} N_b^\phi(\mathbf{x}_\alpha) \boldsymbol{\phi}_b(t) \quad \alpha \in \check{\mathcal{A}} \quad (37)$$

where  $N_b^\varphi$  are the shape functions associated with the micro-rotation field  $\boldsymbol{\varphi}^h$ . For example, we can write the prescribed rotation of ghost particle  $\alpha$  as

$$\boldsymbol{\theta}_\alpha(t) = \boldsymbol{\varphi}^h(\mathbf{x}_\alpha, t) = \sum_{b \in \hat{\mathcal{N}}} N_b^\varphi(\mathbf{x}_\alpha) \boldsymbol{\phi}_b \quad \alpha \in \hat{\mathcal{A}} \quad (38)$$

For all ghost particles (cf. Fig.6), the interpolations can be written as

$$\hat{\mathbf{Q}} = \mathbf{N}_{\hat{Q}D} \mathbf{D} + \mathbf{N}_{\hat{Q}\hat{D}} \hat{\mathbf{D}} \quad (39)$$

where  $\mathbf{N}_{\hat{Q}D}$  and  $\mathbf{N}_{\hat{Q}\hat{D}}$  are shape function matrices containing individual nodal shape functions  $N_a^u$  and  $N_b^\varphi$ , but for now these matrices will be left general to increase our flexibility in choosing interpolation/projection functions (such as those used in meshfree methods). Overall, the particle displacements and rotations may be written as

$$\begin{bmatrix} \mathbf{Q} \\ \hat{\mathbf{Q}} \end{bmatrix} = \begin{bmatrix} \mathbf{N}_{QD} & \mathbf{N}_{Q\hat{D}} \\ \mathbf{N}_{\hat{Q}D} & \mathbf{N}_{\hat{Q}\hat{D}} \end{bmatrix} \cdot \begin{bmatrix} \mathbf{D} \\ \hat{\mathbf{D}} \end{bmatrix} + \begin{bmatrix} \mathbf{Q}' \\ \mathbf{0} \end{bmatrix} \quad (40)$$

where  $\mathbf{Q}'$  is introduced [47] as the error (or “fine-scale” [45]) in the interpolation of the free particle displacements and rotations  $\mathbf{Q}$ , whose function space is not rich enough to represent the true free particle motion. The shape function matrices  $\mathbf{N}$  are in general not square because the number of free particles are not the same as free nodes and prescribed nodes, and number of ghost particles not the same as prescribed and free nodes. A scalar measure of error in particle displacements and rotations is defined as [47]  $e = \mathbf{Q}' \cdot \mathbf{Q}'$ , which may be minimized with respect to prescribed continuum nodal dofs  $\hat{\mathbf{D}}$  to solve for  $\hat{\mathbf{D}}$  in terms of free particle and continuum nodal dofs as

$$\hat{\mathbf{D}} = \mathbf{M}_{\hat{D}\hat{D}}^{-1} \mathbf{N}_{\hat{Q}\hat{D}}^T (\mathbf{Q} - \mathbf{N}_{QD} \mathbf{D}), \quad \mathbf{M}_{\hat{D}\hat{D}} = \mathbf{N}_{\hat{Q}\hat{D}}^T \mathbf{N}_{\hat{Q}\hat{D}} \quad (41)$$

This is known as the “discretized  $L_2$  projection” [47] of the free particle motion  $\mathbf{Q}$  and free nodal dofs  $\mathbf{D}$  onto the prescribed nodals dofs  $\hat{\mathbf{D}}$ . Upon substituting (41) into (39), we may write the prescribed particle dofs  $\hat{\mathbf{Q}}$  in terms of free particle  $\mathbf{Q}$  and continuum nodal  $\mathbf{D}$  dofs. In summary, these relations are written as

$$\hat{\mathbf{Q}} = \mathbf{B}_{\hat{Q}Q} \mathbf{Q} + \mathbf{B}_{\hat{Q}D} \mathbf{D}, \quad \hat{\mathbf{D}} = \mathbf{B}_{\hat{D}Q} \mathbf{Q} + \mathbf{B}_{\hat{D}D} \mathbf{D} \quad (42)$$

where

$$\begin{aligned} \mathbf{B}_{\hat{Q}Q} &= \mathbf{N}_{\hat{Q}\hat{D}} \mathbf{B}_{\hat{D}Q}, & \mathbf{B}_{\hat{Q}D} &= \mathbf{N}_{\hat{Q}D} + \mathbf{N}_{\hat{Q}\hat{D}} \mathbf{B}_{\hat{D}D} \\ \mathbf{B}_{\hat{D}Q} &= \mathbf{M}_{\hat{D}\hat{D}}^{-1} \mathbf{N}_{\hat{Q}\hat{D}}^T, & \mathbf{B}_{\hat{D}D} &= -\mathbf{M}_{\hat{D}\hat{D}}^{-1} \mathbf{N}_{\hat{Q}\hat{D}}^T \mathbf{N}_{QD} \end{aligned} \quad (43)$$

As shown in Fig.6, for a finite element implementation of this dof coupling, we expect that free particle dofs  $\mathbf{Q}$  will not fall within the support of free continuum nodal dofs  $\mathbf{D}$ , such that it can be assumed that  $\mathbf{N}_{QD} = \mathbf{0}$ . The assumption  $\mathbf{N}_{QD} \neq \mathbf{0}$  would be valid for a meshfree projection of the particle motions to the FE nodal dofs, as in [47], where we could imagine that the domain of influence of the meshfree projection could encompass a free particle centroid; the degree of encompassment would be controlled by the chosen support size of the meshfree kernel function. The choice of meshfree projection in [47] was not necessarily to allow  $\mathbf{Q}$  be projected to  $\mathbf{D}$  (and vice versa), but to remove the computationally costly calculation of the

inverse  $\mathbf{M}_{\hat{\mathbf{D}}}^{-1}$  in (42). Since we will also be using the Tahoe code [tahoe.ca.sandia.gov](http://tahoe.ca.sandia.gov) for the coupled multiscale particle-continuum implementation, where the meshfree projection has been implemented for atomistic-continuum coupling [47], we will also consider the meshfree projection in future implementations.

### 3.3.2 Kinetic and potential energy partitioning and coupling

We assume the total kinetic and potential energy and dissipation of the coupled particle-continuum system may be written as the sum of the energies

$$\begin{aligned} T(\dot{\mathbf{Q}}, \dot{\mathbf{D}}) &= T^Q(\dot{\mathbf{Q}}, \hat{\mathbf{Q}}(\dot{\mathbf{Q}}, \dot{\mathbf{D}})) + T^D(\dot{\mathbf{D}}, \hat{\mathbf{D}}(\dot{\mathbf{Q}})) \\ U(\mathbf{Q}, \mathbf{D}) &= U^Q(\mathbf{Q}, \hat{\mathbf{Q}}(\mathbf{Q}, \mathbf{D})) + U^D(\mathbf{D}, \hat{\mathbf{D}}(\mathbf{Q})) \\ F(\dot{\mathbf{Q}}, \dot{\mathbf{D}}) &= F^Q(\dot{\mathbf{Q}}, \hat{\mathbf{Q}}(\dot{\mathbf{Q}}, \dot{\mathbf{D}})) \end{aligned} \quad (44)$$

where we have indicated the functional dependence of the prescribed particle motion and nodal dofs solely upon the free particle motion and nodal dofs  $\mathbf{Q}$  and  $\mathbf{D}$ , respectively. Note that the dissipation function  $F = F^Q$  only applies for the particle system, and only for static problems (dynamic relaxation DE simulation). For purely dynamical problems,  $F^Q = 0$ , and there is only dissipation in the particle system if particles are allowed to slide frictionally, and the continuum has plasticity or other inelastic constitutive response. Lagrange's equations may then be stated as

$$\begin{aligned} \frac{d}{dt} \left( \frac{\partial T}{\partial \dot{\mathbf{Q}}} \right) - \frac{\partial T}{\partial \mathbf{Q}} + \frac{\partial F}{\partial \dot{\mathbf{Q}}} + \frac{\partial U}{\partial \mathbf{Q}} &= \mathbf{F}^{EXT,Q} \\ \frac{d}{dt} \left( \frac{\partial T}{\partial \dot{\mathbf{D}}} \right) - \frac{\partial T}{\partial \mathbf{D}} + \frac{\partial F}{\partial \dot{\mathbf{D}}} + \frac{\partial U}{\partial \mathbf{D}} &= \mathbf{F}^{EXT,D} \end{aligned} \quad (45)$$

which lead to a coupled system of governing equations (linear and angular momentum) for the coupled particle-continuum mechanics. If the potential energy  $U$  is nonlinear with regard to particle frictional sliding and micropolar (or micromorphic) plasticity, then (45) may be integrated in time and linearized for solution by the Newton-Raphson method. The benefit of this multiscale method, as pointed out by Wagner and Liu [45], is that time steps are different for the DE and FE solutions. A multiscale time stepping scheme will follow an approach similar to [45].

## 4 DE-FE facet coupling

This section describes a preliminary method for coupling DE to FE codes, in this case through a single layer of ghost particles tied to FE facets. This is a code communication exercise, to ensure that ELLIP3D [3] can communicate with Tahoe, the DE and FE codes used in the coupling.

### 4.1 DE-FE facet coupling method

A simple granular-continuum coupling scheme is used initially, illustrated in Fig.7. The FE mesh does not cover the entire domain. Instead, the FE and DE regions only overlap through a single layer of particles. This layer of particles is embedded on the surface of the FE domain with centroids constrained to FE facets and deform with FE mesh. We call these particles “ghost” particles, as done in atomistic-continuum coupling methods. Theoretically, the ghost particles can comprise multiple layers and extrude into/overlap with the FE mesh, but this is left for future work [2]. No energy partitioning is currently considered. Only force and kinematics are communicated between the FE and DE regions through the single layer of ghost particles constrained to follow the motion of the FE facets to which they are tied.

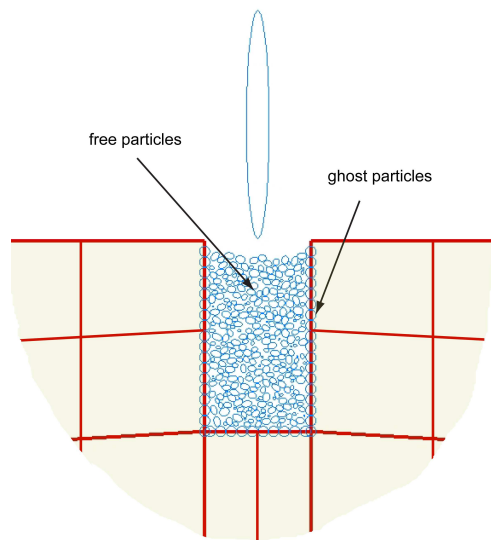


**Fig. 7** Schematic illustration of granular-continuum coupling.

Depending on the FE type, the ghost particles may or may not maintain rotational degree of freedom. Ideally, when a micropolar or micromorphic continuum model is used within the FE region, the ghost particles will have rotational degrees of freedom. If conventional FEM is adopted (like in this section), the ghost particles have constrained rotational degrees of freedom. Free particles in the DE domain carry both translational and rotational degrees of freedom.

The computational framework involves a two-way exchange of information: free particles in the DE simulation contribute to the boundary force in the FE domain through ghost particles, the FE domain provides information needed to compute the boundary condition on the free particles through ghost particles as well. The gran-

ular and continuum scales run simultaneously and exchange relevant information dynamically.

The ghost particles can be placed in such a manner that their centroids are exactly located on the surface FE facets. As ghost particles are discrete in space, the forces are discrete in space as well. Each force acts like a point load on the FE mesh, not necessarily acting at a finite element node. When a point force  $\mathbf{P}$  acts in the interior (including boundary) of the element domain, the relation between the distributed force  $\mathbf{b}(\mathbf{x})$  at point  $\mathbf{x}$  and the point force can be denoted mathematically as

$$\mathbf{b}(\mathbf{x}) = \mathbf{P}\delta(\mathbf{x} - \mathbf{a}) \quad (46)$$

where  $\delta(\mathbf{x} - \mathbf{a})$  is the Dirac delta function and  $\mathbf{x} = \mathbf{a}$  the location of force action  $\mathbf{P}$ . The Dirac delta function has the property that for any vector function  $\mathbf{g}(\mathbf{x})$

$$\int_{\Omega} \mathbf{g}(\mathbf{x})\delta(\mathbf{x} - \mathbf{a})d\mathbf{x} = \begin{cases} \mathbf{g}(\mathbf{a}), & \mathbf{a} \in \Omega \\ \mathbf{0}, & \text{otherwise} \end{cases} \quad (47)$$

Thus the external nodal forces on an element  $e$  arising from a point force  $\mathbf{P}$  at  $\mathbf{a}$  can be obtained by

$$\mathbf{f}^e = \int_{\Omega^e} \mathbf{N}^{eT}(\mathbf{x})\mathbf{b}(\mathbf{x})d\mathbf{v} = \int_{\Omega^e} \mathbf{N}^{eT}(\mathbf{x})\mathbf{P}\delta(\mathbf{x} - \mathbf{a})d\mathbf{v} = \begin{cases} \mathbf{N}^{eT}(\mathbf{a})\mathbf{P}, & \mathbf{a} \in \Omega^e \\ \mathbf{0}, & \text{otherwise} \end{cases} \quad (48)$$

where  $\mathbf{N}^e$  is the matrix of finite element shape functions for element  $e$ . Extending it to all finite elements over the entire domain we have

$$\mathbf{f} = \mathbf{N}^T \mathbf{P} \quad (49)$$

When the FE mesh deforms, the ghost particles move as well, maintaining their centroids on the surface of the FE mesh. Their centroid locations need to be mapped from global coordinates to local element natural coordinates using a Newton-Raphson iterative method. Once the natural coordinates are determined, the locations of ghost particles can be evaluated using the following relationship through shape functions  $\mathbf{N}_{\hat{Q}D}$  during the subsequent simulation:  $\hat{\mathbf{Q}} = \mathbf{N}_{\hat{Q}D} \mathbf{D}$ , where  $(\hat{\bullet})$  denotes prescribed particle dofs. The DE code ELLIP3D is wrapped and integrated into FE code Tahoe using object-oriented programming methodology for the algorithm implementation.

## 4.2 DE-FE facet coupling example

We revisit the penetration motivation example at the beginning of the chapter to demonstrate the effect of having a layer of ghost particles tied to FE facets.

### 4.2.1 Penetration with coupled FE facets

The particles from the penetration example with smaller ‘‘container’’ are combined with a finite element domain, shown in Fig.8.

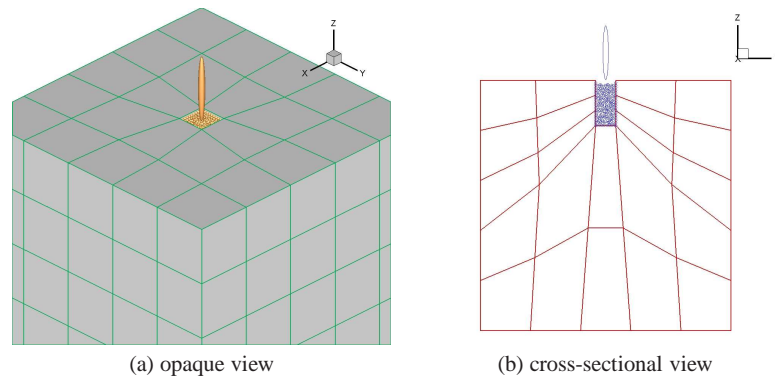


**Fig. 8** 3D view of the DE and FE domains.

As the penetrator particle is driven into the free particles, the ghost particles are squeezed outwards toward the FE domain. Figure 9(a) depicts the penetrator-induced displacement field of all ghost particles (rotations fixed because FE continuum is non-polar). It is noteworthy that the “container” formed by ghost particles swells at lower part, similar to the influence region for geotechnical pile excitation problems.

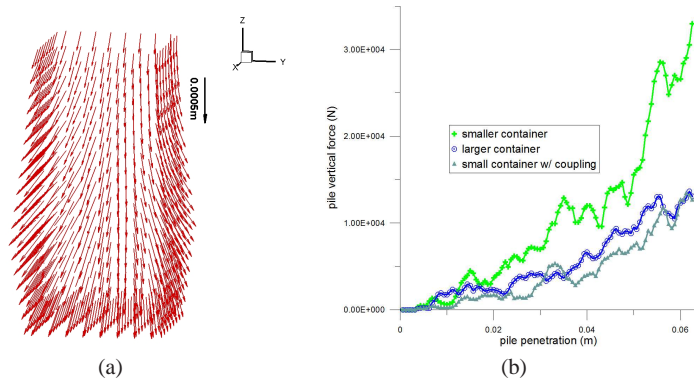


**Fig. 9** (a) Penetrator-induced displacement field of ghost particles using finer mesh. (b) Comparison of force-displacement curves.

To examine the effect of DE-FE coupling on force-displacement curves of penetration, the small container curve and large container curve in Fig.4(c) are plotted again, together with the curve obtained from small container with DE-FE coupling, shown in Fig.9(b). It is observed that the penetrator force of the small container with DE-FE coupling can be tuned to match the larger container with no coupling, by adjusting the elastic compliance of the FE continuum surrounding the container. The boundary effect difference shown in Fig.4(c) can be partially or completely elimi-

nated by applying a more robust DE-FE coupling technique in future work, similar to the atomistic-continuum coupling methods, but accounting for differences with granular materials (see Section 3.3). Such work is ongoing.

## 5 Summary

The chapter presented a concurrent multiscale computational method for modeling at the grain-scale the interfacial mechanics between dense dry granular materials and deformable solid bodies. Section 3 presented the formulation for coupling particle and micropolar continuum mechanics regions of a granular material, following the lattice-structure-based approaches described in [45, 47], but extending to rotational dofs, and consideration of free particle domain  $\mathcal{B}^{DE}$  with no overlain FE mesh. For the case of large particle motion and frictional sliding in the overlap region  $\mathcal{B}^h \cup \mathcal{B}^h$ , a finite deformation micromorphic plasticity model is needed to couple to the particle mechanics and is presented in [54, 55]. Section 4 presented a preliminary DE-FE coupling via single ghost layer of particles tied to FE facets, which demonstrates a code communication between the DE and FE codes being used in the research.

## 6 Ongoing and future work

Various aspects of the research on ongoing, while others are considered for future work. Ongoing research includes: (1) implementing the micromorphic elastoplasticity model into Tahoe; (2) coupling the micromorphic FE to the DE code through an overlapping region; and (3) testing the computational implementations for a penetration example and other granular soil-solid body interface problems.

Future research entails: (4) extend micromorphic pressure sensitivity plasticity to more advanced constitutive models, such as critical state plasticity and including particle breakage; (5) address adaptivity of the multiscale scheme to be able to convert continuum to particle as a solid body shears through a granular material, or particle to continuum in particle regions that behave more like a continuum; and (6) extend to multiphase mechanics (solid grains, pore liquid and gas).

**Acknowledgements** The authors acknowledge the support of NSF grant CMMI-0700648.

## References

1. Cone penetrometers. <http://geosystems.ce.gatech.edu/Faculty/Mayne/Research/devices/cpt.htm>
2. R. Regueiro, in *Proc. IMECE2007* (Seattle, WA, USA, 2007), 42717, pp. 1–6

3. B. Yan, R. Regueiro, S. Sture, Three dimensional discrete element modeling of granular materials and its coupling with finite element facets (2010). In press, Eng. Comput.
4. O. Reynolds, Philosophical Mag. J. Science **20**(127), 469 (1885)
5. P. Newland, B. Allely, Geotechnique **7**, 17 (1957)
6. P. Rowe, Proc. R. Soc. Lond. A, Math. Phys. Eng. Sci. **A269**, 500 (1962)
7. S. Cowin, M. Satake, *Continuum Mechanical and Statistical Approaches in the Mechanics of Granular Materials* (Gakujutsu Bunken Fukyu-Kai, Tokyo, 1978)
8. J. Jenkins, M. Satake, *Mechanics of Granular Materials* (Elsevier Science, 1983)
9. M. Satake, e. J.T. Jenkins, *Micromechanics of Granular Materials* (Elsevier Science, 1988)
10. e. C.S. Chang, et al., *Mechanics of Deformation and Flow of Particulate Materials* (American Society of Civil Engineers, 1997)
11. e. D. Kolymbas, *Constitutive Modelling of Granular Materials* (Springer, 2000)
12. J. Duffy, H. Deresiewicz, J. App. Mech. **24**(4), 585 (1957)
13. H. Deresiewicz, Adv. App. Mech. **5**, 233 (1958)
14. J. Christoffersen, M. Mehrabadi, S. Nemat-Nasser, J. App. Mech. **48**, 339 (1981)
15. L. Rothenburg, A. Selvadurai, in *Mechanics of Structured Media*, ed. by A. Selvadurai (Elsevier Scientific, 1981), pp. 469–486
16. J. Goddard, Y. Bashir, in *Recent Developments in Structured Continua*, ed. by D. DeKee, P. Kaloni (Longman Scientific and Technical, J. Wiley, 1990), pp. 23–35
17. C. Chang, Y. Chang, M. Kabir, ASCE J. Geotech. Eng. Div. **118**(12), 1959 (1992)
18. B. Gardiner, A. Tordesillas, Int. J. Solids Struct. **41**(21), 5885 (2004)
19. S. Luding, Int. J. Solids Struct. **41**(21), 5821 (2004)
20. J. Peters, J. Eng. Math. **52**(1-3), 231 (2005)
21. K.I. Kanatani, Int. J. Engr. Sci. **17**(4), 419 (1979)
22. C. Chang, C. Liao, Int. J. Solids Struct. **26**, 437 (1990)
23. J. Bardet, J. Proubet, J. Eng. Mech. **118**(2), 397 (1992)
24. H.B. Muhlhaus, F. Oka, Int. J. Solids Struct. **33**(19), 2841 (1996)
25. W. Ehlers, S. Diebels, W. Volk, J. Phy. **8**(8), 127 (1998)
26. A. Suiker, R. De Borst, C. Chang, Acta Mech. **149**(1-4), 161 (2001)
27. A. Tordesillas, D. Walsh, Powder Technol. **124**(1-2), 106 (2002)
28. A. Suiker, C. Chang, J. Eng. Mech. **130**(3), 283 (2004)
29. S. Walsh, A. Tordesillas, Acta Mech. **167**(3-4), 145 (2004)
30. E. Pasternak, H.B. Muhlhaus, J. Eng. Math. **52**(1), 199 (2005)
31. B. Gardiner, A. Tordesillas, Powder Technol. **161**(2), 110 (2006)
32. A. Eringen, *Microcontinuum Field Theories I: Foundations and Solids* (Springer-Verlag, 1999)
33. P. Cundall, O. Strack, Geotechnique **29**, 47 (1979)
34. J. Williams, Eng. Comput. **5**(3), 198 (1988)
35. J. Bardet, J. Proubet, Comput. Struct. **39**(3/4), 221 (1991)
36. Y. Bashir, J. Goddard, J. Rheol. **35**, 849 (1991)
37. A. Anandarajah, ASCE J. Geotech. Eng. Div. **120**(9), 1593 (1994)
38. R. Borja, J. Wren, Comp. Meth. App. Mech. Engr. **127**(1-4), 13 (1995)
39. Wren, J.R. and Borja, R.I., Comp. Meth. App. Mech. Engr. **141**(3–4), 221 (1997)
40. S. Luding, M. Latzel, W. Volk, S. Diebels, H. Herrmann, Comp. Meth. App. Mech. Engr. **191**(1-2), 21 (2001)
41. K. Han, D. Peric, A. Crook, D. Owen, Eng. Comput. **17**(2), 593 (2000)
42. M. Kremmer, J. Favier, Int. J. Numer. Methods Eng. **51**(12), 1407 (2001)
43. P. Komodromos, J. Williams, Eng. Comput. **21**(2-4), 431 (2004)
44. H. Nakashima, A. Oida, J. Terramech. **41**(2-3), 127 (2004)
45. G. Wagner, W. Liu, J. Comput. Phys. **190**(1), 249 (2003)
46. S. Xiao, T. Belytschko, Comp. Meth. App. Mech. Engr. **193**(17-20), 1645 (2004)
47. P. Klein, J. Zimmerman, J. Comput. Phys. **213**(1), 86 (2006/03/20)
48. F. Feyel, J.L. Chaboche, Comp. Meth. App. Mech. Engr. **183**, 309 (2000)
49. T. Belytschko and S. Loehnert and J.-H. Song, Int. J. Numer. Methods Eng. **73**, 869 (2008)
50. F. Feyel, Comp. Meth. App. Mech. Engr. **192**, 3233 (2003)
51. J. Rayleigh, *The Theory of Sound. Volume 1*, 1st edn. (Dover Pub. Inc., New York, 1945)

52. A. Eringen, *Theory of Micropolar Elasticity* (Academic Press, New York, 1968), *Fracture, An Advanced Treatise*, vol. 2, 1<sup>st</sup> edn., Chap. 7, pp. 622–729
53. T.J.R. Hughes, *The Finite Element Method* (Prentice-Hall: New Jersey, 1987)
54. R. Regueiro, *Int. J. Solids Struct.* **47**, 786 (2010)
55. R. Regueiro, *J. Eng. Mech.* **135**, 178 (2009)